Energy &
Environmental
Science

Accepted Manuscript

ROYAL SOCIETY OF CHEMISTRY

www.rsc.org/ees

Industrially scalable and cost-effective Mn^{2+} doped $Zn_xCd_{1-x}S/ZnS$ nanocrystals with 70% photoluminescence quantum yield, as efficient down-shifting material in photovoltaics

I. Levchuk[†,§], C.Würth[‡,], F. Krause[†], A. Osvet[†], M. Batentschuk[†,], U. Resch-Genger[‡*], C. Kolbeck[#],*
P. Herre[@], H.P. Steinrück[#],W. Peukert[@] and C. J. Brabec[†,§,⊥]

† Friedrich-Alexander-Universität Erlangen-Nürnberg, Materials for Electronics and Energy Technology (i -MEET), Martensstraße 7, 91058 Erlangen, Germany

‡ Division Biophotonics, BAM Federal Institute for Materials Research and Testing, Richard-Willstaetter-Str. 11, D-12489 Berlin, Germany

§ Energy Campus Nürnberg (EnCN), Fürther Str. 250, 90429 Nürnberg, Germany

⊥ ZAE Bayern, Renewable Energies, Haberstr. 2a, 91058 Erlangen, Germany

Chair of Physical Chemistry II, University of Erlangen-Nürnberg, Egerlandstr. 3, 91058 Erlangen, Germany

@ Institute of Particle Technology, Friedrich-Alexander-Universität Erlangen-Nürnberg, Cauerstraße 4, 91058 Erlangen, Germany

Keywords: one pot synthesis; doped nanocrystals; photoluminescence quantum yield; down-shifting; solar energy conversion; solar cell;

*Address correspondence to: miroslaw.batentschuk@fau.de, ute.resch@bam.de

Abstract

We present colloidally stable and highly luminescent $Zn_xCd_{1-x}S$:Mn/ZnS core-shell nanocrystals (NCs) synthesized via a simple non-injection one-pot, two-step synthetic route, that can be easily upscaled. Systematic variation of the reaction component, parameters and thickness of the ZnS shell yielded doped nanocrystals with a very high photoluminescence quantum yield (Φ_{pl}) of 70 %, which is the highest value yet reported for this Mn-doped sulfide-semiconductor NCs. These materials can be synthesized with high reproducibility in large quantities of the same high quality, i.e., same Φ_{pl} using accordingly optimized reaction conditions. Application of these zero-reabsorption high quality NCs in the light conversion layers, deposited on top of a commercial monocrystalline silicon (mono-Si) solar cell, led to a significant enhancement of the external quantum efficiency (EQE) of this device in the ultraviolet spectral region between 300 and 400 nm up to ca. 12 %. The EQE enhancement is reflected by an increase in the power conversion efficiency (PCE) by nearly 0.5 percentage points and approached the theoretical limit (0.6%) expected from down-shifting for this Si solar cell. The resulting PCE may result in a BoM (bill of materials) cost reduction of app. 3 % for mono-Si photovoltaic modules. Such small but distinct improvements are expected to pave the road for an industrial application of doped semiconductor NCs as cost-effective light converters for silicon photovoltaics (PV) and other optoelectronic applications.

Introduction

During the past decades, doped semiconductor quantum dots (d-dots) have been increasingly studied since they retain nearly all intrinsic advantages of quantum dots (QDs) and benefit from larger Stokes shifts, minimum reabsorption, and longer excited state lifetimes related to dopant emission.[1] Especially Mn^{2+}-doped chalcogenide nanocrystals (NCs)[2,3] together with Cu^{+}-doped materials of the same composition[4,5] have the potential to become a new class of emissive nanomaterials with high application potential as optical reporters in bioanalysis and active components in optical devices like solar cells. This, however, correlates with advances in synthetic routes that yield high quality d-dots with a photoluminescence quantum yield (Φ_{pl}) of at least 50 % with a high reproducibility and can be upscaled.

One of the best studied d-dots are Mn^{2+}-doped Zn and Cd chalcogenide NCs and their alloys.[1] The luminescence of these NCs is governed by the $^4T_1$–$^6A_1$ emission of Mn^{2+} in the orange wavelength region of 580-600 nm, which is nearly independent of the host material and crystal size. These d-d transitions are spin and parity forbidden, which leads to small absorption cross sections, hindering direct optical excitation, and a long intrinsic luminescence lifetime in the order of milliseconds. The absorption properties of these doped NCs are largely determined by the host matrix, which - together with an efficient energy transfer from the host to the Mn^{2+} ions - ensures bright photoluminescence. As photon absorption occurs mainly by the host lattice, the luminescence properties of doped QDs are similarly sensitive to surface defects like conventional semiconductor NCs, rendering the passivation of surface states, which favor non-radiative relaxation of the charge carriers formed upon light absorption, the main factor controlling Φ_{pl} of these d-dots. Surface state passivation can be achieved by a crystalline shell of a wide bandgap semiconductor like ZnS.[6] Moreover, the shell material can enable band gap engineering to control the location of the charge carriers photogenerated in the core.[7] Yang et al.[8] recently presented a detailed study on factors governing the PL of Mn^{2+}-doped CdS/ZnS core-shell NCs including the influence of the spatial localization of Mn^{2+} ions inside core-shell QDs as well as the role of surface trap states and energy transfer mechanisms. In this respect, they also reported a surface modification procedure to eliminate surface states, which yielded Mn^{2+}-doped NCs with a Φ_{pl} in the order of 50 %. This is the first example of d-dots with a Φ_{pl} comparable to common undoped $A^{II}B^{VI}$ core–shell QDs.[8,9,10]

The synthesis of highly luminescent doped NCs requires reproducible and eventually up-scalable procedures which enable control of all parameters affecting crystal growth and incorporation of doping ions as well as proper surface passivation. Presently, high-quality doped QDs are efficiently synthesized via high temperature synthetic routes to minimize the formation of surface defects.[1] It is, however, challenging to incorporate dopant ions into a host QD lattice without simultaneously reducing the Φ_{pl} due to the size mismatch between host cations and dopant ions (e.g., the ion radius of Mn^{2+}, 0.85 Å, differs from that of Zn^{2+}, i.e., 0.75 Å, and Cd^{2+}, i.e., 0.95 Å)[11] and the ‘‘self-purification’’ effect.[12] A key factor for obtaining high-quality doped QDs is the timing of dopant addition.[13] There are three strategies to introduce dopant ions into host QDs: dopant introduction together with the host precursors,[14-16] before nucleation of the host material,[2,3] and during shelling of the host QD.[17] Methods for the direct introduction of Mn^{2+} ions into a growing core or shell are very sensitive to different synthetic parameters and hence, frequently suffer from reproducibility problems. As a new approach to the synthesis of Mn^{2+}-doped QDs, here exemplarily for ZnSe systems, Pradhan et al. utilized the initial formation of MnSe seeds followed by chemical substitution of Mn by Zn at a higher temperature in organic solvents.[2] For Mn^{2+}-doped ZnSe core NCs with a ZnS or ZnSe shell, with this method Φ_{pl} up to values 60 % could be realized,[18,19] yet this required a complicated multistep hot injection phosphine strategy. In the case of injection-based methods, several kinetic and thermodynamic factors such as temperature instability, mixture heterogeneity, and overall high reaction rates and limited mass-transfer rates, however, often hinder the reproducible preparation of high quality nanocrystals with high Φ_{pl} on a large scale. Injection-based shelling methods involving the gradual injection of shell precursors at elongated temperatures, can allow the formation of gradient core–shell QDs with a smooth potential barrier for electrons and holes, without strains or interfacial defects, and, as a consequence, a Φ_{pl} approaching 100% as recently shown for undoped II-VI semiconductor QDs.[20] This can be also utilized to introduce dopant ions during shelling of the host QD. Alternatives present non-injection syntheses.[21] Such methods have been reported also for the preparation of Mn^{2+}-doped CdS/ZnS[8], CuInS/ZnS[22] and MnS/ZnS/CdS[23] core-shell QDs, yielding brightly emitting doped QDs with Φ_{pl} of 56 to 68 %. These non-injection methods require, however, several steps to obtain the final high quality products, which hampers upscaling.

The application of very promising Mn-doped QDs as fluorescent reporters and active material in white light emitting diodes and spectral converters in photovoltaics (PV) [24,25,26] calls for simple and reproducible synthetic procedures using inexpensive precursors that yield high amounts of strongly luminescent NCs. This can be best met with a one-pot approach. The Φ_{pl} of Mn^{2+}-doped QDs synthesized via one pot reactions are presently, however, still comparatively low, with maximum Φ_{pl} values of 30 %.[27,24] This is ascribed to the general challenge to incorporate Mn^{2+} into the host lattice and insufficient passivation of surface defects.[11]

In this paper we present an industrially scalable and cost-effective one-pot, two-step non-injection synthesis for highly luminescent $Zn_xCd_{1-x}S$:Mn/ZnS NCs. A consequent optimization of the synthetic route for the NC core synthesis as well as for the surface passivation with a ZnS shell allowed to achieve the highest Φ_{pl} reported to date for this material.

To underline the application potential of the these nanoparticles, doped NCs with high Φ_{pl} were subsequently used for the fabrication of down-shifting layers and coupled to monocrystalline silicon (mono-Si) solar cells, resulting in an enhanced external quantum efficiency (EQE) in the UV- blue spectral range and an overall higher AM1.5 power conversion efficiency (PCE). The industrial relevance of this approach was carefully examined by performing a BoM (bill of materials) and BoS (bill of system) analysis for NC based PL conversion layers for mono-Si modules.

Experimental section

Chemicals. Zinc acetate ($Zn(OAc)_2$, 99.99%), cadmium oxide (CdO, 99.99+%), manganese acetate ($Mn(OAc)_2$, 99.99%), sulfur powder (99.99%), dodecanethiol (DDT, 99.9%), oleic acid (OA, 90%), oleylamine (OAm, 70%, technical grade), and 1-octadecene (ODE, 90%) were purchased from Sigma-Aldrich. All chemicals were used without further purification. $Zn_{1-x}Cd_xS$:Mn and the core/shell NCs were synthesized based on a previously reported protocol[4] with slight modifications.

Preparation of stock solutions. The Zn, Cd, and Mn stock solutions were prepared in an air-free glovebox. The. 0.1 M Zn stock solution was obtained by dissolving 0.220 g (1 mmol) of $Zn(OAc)_2$ in 0.8 mL of OAm, and 9.2 mL of ODE at 160 °C. For the 0.1 M Cd stock solution, 0.128 g (1 mmol) of CdO were dissolved in 2.0 mL of OA, and 8.0 mL of ODE at 160 °C. The 0.01 M Mn stock solution was prepared by dissolving 0.017 g (0.05 mmol) of $Mn(OAc)_2$ in 1 mL of OAm, and 9 mL of ODE at 80 °C. For the preparation of the ZnS shell, we used a 0.4 M Zn stock solution, made by dissolving 0.878 g (4 mmol) of $Zn(Ac)_2$ in 3.0 mL of OAm and 7 mL of ODE at 160 °C. The 0.4 M ODE-S solution was obtained by dissolving 0.128 g of sulfur (4.0 mmol) in 10.0 mL of ODE at 160 °C. All stock solutions were stored at 50 °C in a glovebox before use.

Synthesis of $Zn_xCd_{1-x}S$:Mn NCs. All syntheses were carried out using Schlenk line under nitrogen atmosphere; isolation and purification of the NCs were carried out in air. In a typical procedure, 1 ml DDT and 2 ml ODE were filled into a 50-mL three-neck flask in a heating mantle, heated to 40 °C under vacuum, and kept under these conditions for 1 hour to remove oxygen and water. Then, the reaction mixture was cooled to room temperature and purged with nitrogen. Subsequently, 1.0 mL of a 0.1 M Zn stock solution (0.1 mmol), 1.0 mL of a 0.1 M Cd stock solution (0.1 mmol), 1 mL of a 0.01 M Mn stock solution (0.01 mmol), and 1.0 mL of a 0.4 M ODE-S solution (0.4 mmol) were added. The reaction mixture was heated to 230 °C with a heating rate of 12 °C/min under nitrogen flux and kept at this temperature to grow $Zn_xCd_{1-x}S$:Mn NCs. For the monitoring of the reaction and the optimization of the reaction parameters with respect to the optical properties of our NCs, aliquots of the NCs dispersion were taken at different reaction times, injected into cold toluene to terminate the NC growth, and then diluted with chloroform for the spectroscopic measurements. After completion of NC growth, the reaction mixture was cooled to 60 °C and 10 ml of toluene or chloroform was added. The NCs were precipitated by addition of an excess of ethanol, removed from the dispersion by centrifugation (8000 rpm, 10 min), and purified four times by a precipitation/re-dispersion method using a solvent mixture of chloroform and ethanol (2/4 volume mixture). The purified NCs were then re-dispersed in chloroform. To obtain $Zn_xCd_{1-x}S$:Mn NCs with different Zn/Cd ratios, the Zn/Cd precursor ratio was varied while all other variables were kept constant.

Deposition of ZnS shell. Shelling of the $Zn_xCd_{1-x}S$:Mn cores with different layers of ZnS was performed with the crude Mn:$Zn_xCd_{1-x}S$ reaction mixture after reaching temperature to 230°C when the emission of the core NCs was maximum. 3.0 ml of a 0.4M stock solution of the Zn precursor were injected into the reaction mixture in 0.5 ml portions drop by drop at time intervals of 15 min. For the monitoring and optimization of the shelling procedure with respect to maximum NCs brightness, NCs aliquots were taken before injection of a new portion of Zn stock solution and spectroscopically studied in chloroform. Purification of $Zn_xCd_{1-x}S$:Mn/ZnS NCs was performed similarly to that of the $Zn_xCd_{1-x}S$:Mn NCs.

Scaling up of the NCs synthesis. The amount of all components used for the previously described synthesis of $Zn_xCd_{1-x}S$:Mn were increased 40 times. Briefly, 40 ml DDT and 80 ml ODE were filled into a 500-ml three-neck flask and heated to 40°C under vacuum. At room temperature, 40 m of a 0.1 M Zn stock solution (4 mmol), 40 ml of a 0.1 M Cd stock solution (4 mmol), 40 ml of 0.01 M Mn stock solution (0.4

mmol), and 40 ml of a 0.4 M ODE-S solution (16 mmol) were added. The reaction mixture was heated to 230 °C to obtain $Zn_xCd_{1-x}S$:Mn NCs. For the coating with a ZnS Shell, the entire stock solution of the 0.4M Zn precursor (120 ml) was injected in six 10 ml portions drop by drop into the reaction vessel at intervals of 15 min at 230 °C. After completion of particle growth, the reaction mixture was cooled to 60 °C and 250 ml of toluene or chloroform were added. Purification was performed as previously described, taking into account the upscaling factor.

Deposition of the down-shifting layer. NCs were deposited directly onto the surface of 41 x 19.5 x 0.3 mm solar cells (LEMO-SOLAR GmbH), previously cleaned with ethanol and dried, using a doctor blade technique. For the preparation of the coating solutions from different concentrations of $Zn_xCd_{1-x}S$:Mn/ZnS NCs, the NCs were precipitated from chloroform dispersions by addition of ethanol. The separated NCs were dried overnight in a vacuum oven and subsequently dispersed in toluene with different amounts, here 0.5-25 mg/ml. For the NC deposition, the temperature of the doctor blade hot plate was set to 40 °C, the blade gap was set to 400 μm, and 200 μl of each solution were coated with a speed of 10 mm/s. After NC coating, all solar cells were annealed at 80 °C for five min. to remove traces of organic solvent.

Material characterization

Energy-Dispersive X-ray spectroscopy (EDX). Elemental analysis of the NCs was done with a Philips ESEM XL30 scanning electron microscope equipped with a field emission gun and operated at 10 kV.

Transmission electron microscopy (TEM) and high resolution electron microscopy (HRTEM). TEM and HRTEM images were recorded with a PHILIPS CM 300 UT high-resolution transmission electron microscope (300 kV acceleration voltage, 0.172 nm point resolution – Scherzer focus) equipped with two-cameras (TV System and CCD camera). Samples for TEM were prepared by casting one drop of the NC dispersion onto a standard carbon film on copper grid (230 meshes).

X-ray Powder Diffraction (XRD). X-ray diffraction measurements were carried out with Siemens D500 X-ray diffractometer with Cu Kα radiation (λ= 1.5406 Å). Before each measurement, the purified NCs were dried in a vacuum oven at 60 °C overnight.

Fourier transform infrared spectroscopy (FTIR). FTIR measurements were done with a VERTEX-70 spectrometer (Bruker Optik GmbH).

Scanning Electron Microscopy (SEM). Images were taken with a FEI-Quanta 200 scanning electron microscope at an operation voltage of 20 kV.

X-ray photoelectron spectroscopy (XPS). The XP spectra were collected using a non-monochromated Mg K_α anode operated at a power of 238 W, and an Omicron Argus electron analyzer; the pass energy was set to 200 eV for survey spectra and to 35 eV for detail spectra. The binding energy axis is referenced to the C 1s signal at 285.0 eV. The samples investigated by XPS were prepared by dripping the NC dispersion on a Mo-based sample holder, which was transferred to the XPS chamber using a load-lock system. To remove residual solvent, the sample was heated to 60°C in situ prior to the measurement.

Optical measurements. Absorption spectra of the NC dispersions were taken on a Perkin-Elmer Lambda 950 spectrometer and emission spectra on a Jasco Spectrofluorometer FP-8500. The emission spectra shown were corrected for the wavelength-dependent spectral responsivity of the fluorometer.

Lifetime measurements. The photoluminescence decay curves were measured by exciting the dispersed nanoparticle samples by a pulsed Xe lamp (pulse width 4 µs) through a 360 nm bandpass filter. The emission was dipersed by an H10 monochromator (Jobin-Yvon), detected with a 9816 photomultiplier (EMI) and recorded with a digital oscilloscope TDS540 (Tektronix).

Measurement of Φ_pl. Φ_pl were measured absolutely with a calibrated integrating sphere setup at BAM previously reported.[54,55]This involves the determination of the absorbed photon flux ($q_\mathrm{p}^{abs}(\lambda_\mathrm{em})$) and the emitted photon flux ($q_\mathrm{p}^{em}(\lambda_\mathrm{em})$) by a sample (see eq. 1) with an integrating sphere setup.[54]

$$\Phi_\mathrm{pl} = \frac{\displaystyle\int_{\lambda_{\mathrm{em}_1}}^{\lambda_{\mathrm{em}_2}} \frac{\left(I_\mathrm{x}(\lambda_\mathrm{em}) - I_\mathrm{b}(\lambda_\mathrm{em})\right)}{s(\lambda_\mathrm{em})}\,\lambda_\mathrm{em}\,d\lambda_\mathrm{em}}{\displaystyle\int_{\lambda_{ex}-\Delta\lambda}^{\lambda_{ex}+\Delta\lambda} \frac{\left(I_\mathrm{b}(\lambda_\mathrm{ex}) - I_\mathrm{x}(\lambda_{ex})\right)}{s(\lambda_{ex})}\,\lambda_\mathrm{ex}\,d\lambda_\mathrm{ex}} = \frac{q_\mathrm{p}^\mathrm{pl}}{q_\mathrm{p}^\mathrm{abs}} \tag{1}$$

The emitted photon flux follows from the blank and spectrally corrected emission spectrum of the sample ($I_\mathrm{x}(\lambda_\mathrm{em})$) integrated over the emission band. The absorbed photon flux is calculated from the difference between the transmitted excitation light with the blank ($I_\mathrm{b}(\lambda_\mathrm{ex})$) and the sample ($I_\mathrm{x}(\lambda_\mathrm{ex})$), within the wavelength region of the excitation bandwidth. $s(\lambda_\mathrm{em})$ and $s(\lambda_\mathrm{ex})$ represent the spectral responsivity of the detection system in the spectral regions of emission and excitation.

Solar cell characterization. A solar simulator (Oriel Sol 1A, Newport) with an AM1.5G spectrum operated at 100 mW cm^{-2} was used for illumination of the solar cells. A source measurement unit (Botest LIV) was used to record the current-voltage curves. EQE measurements were carried out with a quantum efficiency (QE) measurement system QE-R from Enlitech.

Result and discussions

Synthesis of doped NCs. The phosphine-free synthesis of $Zn_xCd_{1-x}S$:Mn/ZnS core/shell NCs was performed via a non-injection route based on a doping technique utilizing nucleation, where the starting materials for the core of the NC and the dopant precursor are loaded together into the reaction vessel at room temperature. The main steps of this synthesis, which is based on a modified method by Zhang et al.[4] for $Zn_xCd_{1-x}S$:Cu, are shown in Figure 1 and subsequently described; more details are given in the *Experimental* section. The PL mechanism of Mn-doped NCs is completely different from the one of Cu-doped NCs. In the case of Cu doping, electrons from the conduction band of the host material recombine with holes in the Cu-mediated state. Different to this, Mn doping leads to a recombination process within d-d levels of Mn^{2+}. Therefore, a deep and systematic revision of the previously reported synthetic approach[4] for Cu-doped $Zn_xCd_{1-x}S$ NCs was required. We fabricated highly regular Mn^{2+} doped $Zn_xCd_{1-x}S$ NCs which were further effectively passivated with a ZnS shell and report here for the first time the synthesis methods and the extended characterization.

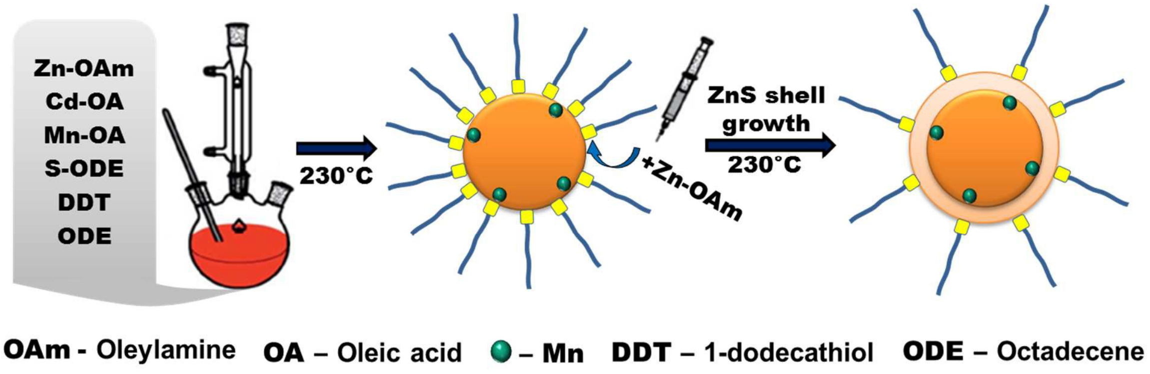

Figure 1. Schematic illustration of the one pot, two step synthesis of $Zn_xCd_{1-x}S$:Mn/ZnS core-shell NCs.

A mixture of the solvents dodecanethiol (DDT) and octadecene (ODE) was degassed, stock solutions of the Zn, Cd, and Mn-precursors as well as an ODE-sulfur solution were added, and the reaction mixture was heated to 230 °C under nitrogen flow and continuous stirring. After completion of the particle growth, the reaction mixture was cooled to 60 °C. The resulting doped NCs were precipitated by addition of ethanol and purified by a precipitation/re-dispersion method. For control of the synthesis and optimization of the reaction conditions, aliquots of the reaction mixture were taken at different temperatures and times and spectroscopically studied. The growth experiments were made mainly with a Zn/Cd/Mn precursor ratio of 50/50/5, which was the first parameter optimized with this procedure.

Structural characterization. The results of the structural characterization of the $Zn_xCd_{1-x}S$:Mn NCs with transmission electron microscopy (TEM), X-ray diffraction (XRD) and Fourier transform infrared spectroscopy (FTIR) are summarized in Figures 2a-2e. All NCs reveal a near-spherical shape and possess high size uniformity (Figures 2a and 2b). The size of the nanoparticles was estimated from transmission electron microscopy (TEM) to be 2.88±0.4 nm with a size distribution of only 14% and 3.23±0.42 nm with size distribution of 13% for $Zn_{0.5}Cd_{0.5}S$:Mn and $Zn_{0.5}Cd_{0.5}S$:Mn/ZnS, respectively. Interplanar spacing in the single nanoparticles was obtained by high resolution transmission electron microscopy (HRTEM) analysis. In both, core and core/shell NCs the interplanar spacing is 0.32 nm, which is in between the spacing for CdS (0.33544 nm) and ZnS (0.31261) for the 111 plane of the cubic structure. Wide-angle XRD patterns summarized in Figure 2c reveal the phase and elemental composition of representatives $Zn_{0.5}Cd_{0.5}S$:Mn core NCs (lower spectrum) and $Zn_{0.5}Cd_{0.5}S$:Mn/ZnS core/shell NCs (upper spectrum) samples, which display the characteristic peaks of the zinc blende (cubic) structure, located between those of cubic ZnS and CdS materials, respectively. This confirms the $Zn_{0.5}Cd_{0.5}S$ alloy structure. Coating the ZnS shell over $Zn_{0.5}Cd_{0.5}S$ core also slightly changed the lattice constant from 5.57 to 5.50 Å. Due to the similar lattice parameter of the ZnS and $Zn_{0.5}Cd_{0.5}S$ and a likely atomic diffusion at the core/shell interface, it was not possible to differentiate the core from the shell by HRTEM. This phenomen is well known for different kinds of core/shell structures, such as Ag/Au[57], $NaYbF_4$:Er/$NaYF_4$[58] or CdSe-Core CdS/$Zn_{0.5}Cd_{0.5}S$/ZnS[5] multishell nanocrystals. The crystallite size for $Zn_xCd_{1-x}S$:Mn and $Zn_xCd_{1-x}S$:Mn/ZnS thin powder layers was determined from the XRD pattern to be 3.05 and to 3.5 nm by a

Gaussian fit and the Debye-Scherrer formula, respectively. This is in excellent agreement with the results from HRTEM.

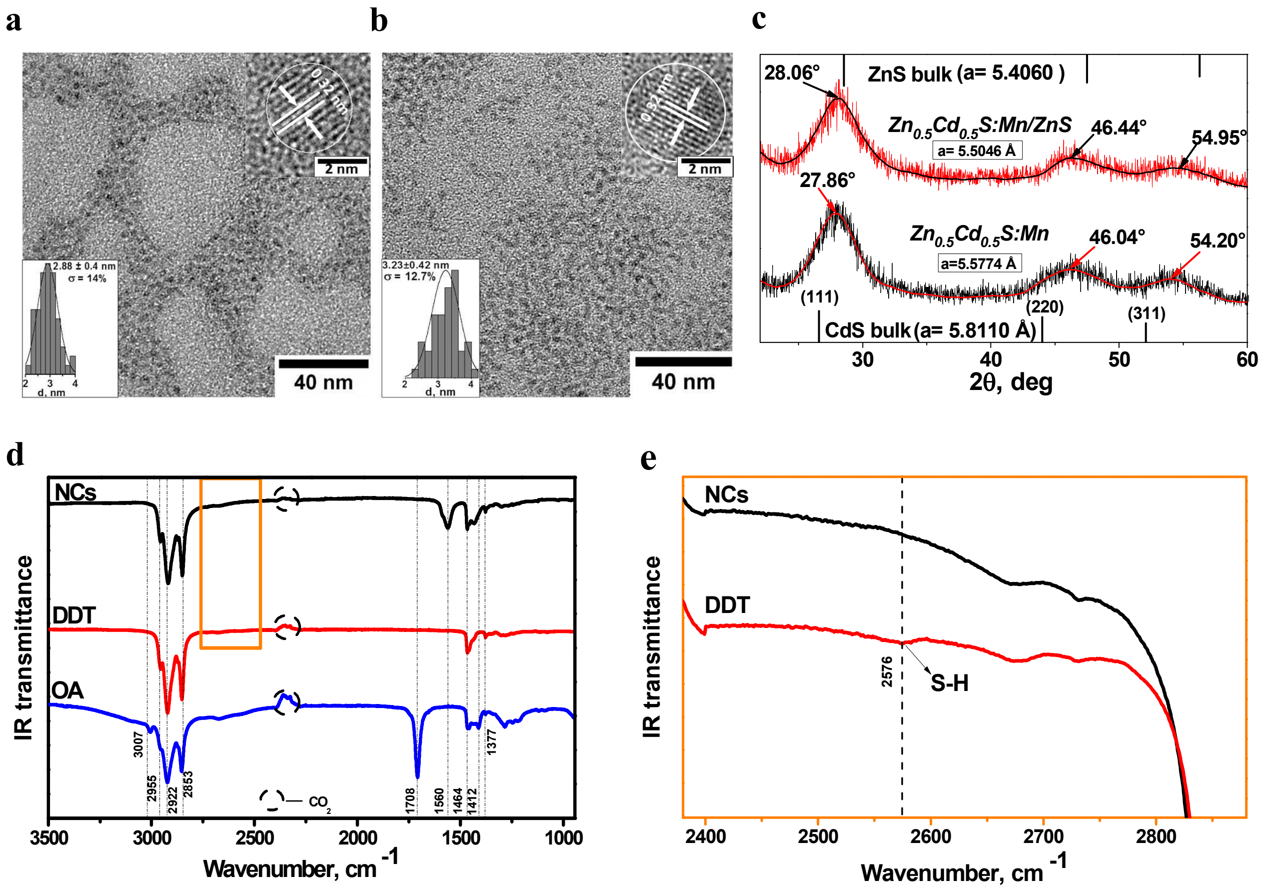

Figure 2. TEM and HRTM images of (a) Zn$_{0.5}$Cd$_{0.5}$S:Mn and (b) ZnS-coated Zn$_{0.5}$Cd$_{0.5}$S:MnNCs; the corresponding size distributions obtained by TEM are given as insets. (c) XRD patterns of the two NC samples. The standard data for ZnS zinc blende bulk material (top, ICSD 00-005-0566) and zinc blende bulk CdS (bottom, ICSD pattern 01-080-0019) are shown as reference. (d) FTIR spectra of Zn$_{0.5}$Cd$_{0.5}$S:Mn(5%)/ZnS NCs, and (e) an enlarged view of the same spectra in the wavelength region of 2380-2880 cm^{-1} for the NCs and DDT.

FTIR spectra of purified Zn$_{0.5}$Cd$_{0.5}$S:Mn(5%)-ZnS NCs shown in Figure 2d and 2e provide information on the surface chemistry of the doped QDs. The bands in the range of 3000 to 2800 cm^{-1} are attributed to C-

H stretching vibrations of dodecanethiol (DDT) and oleic acid (OA) and to the asymmetric vibration of CH_3 (2955 cm^{-1}) as well as the asymmetric (2922 cm^{-1}) and symmetric stretching of CH_2 (2853 cm^{-1}), respectively. The peak at 1708 cm^{-1} is ascribed to the C=O stretch vibrations of OA. The band at 1560 cm^{-1} corresponds to carboxylate groups of the OA ligands and provides evidence of a coordinative bond between this group and Zn^{2+} or Cd^{2+} cations on the NC surface.[28] Comparison of the IR spectra of pure DDT and the NCs samples (Figure 2, panel e) shows that the weak S-H vibrational band at 2576 cm^{-1} found in DDT is absent in the NCs. This confirms the broken S-H bonds due to chemisorption of thiolates onto the surface of the NCs.[29,30] Hence, DDT serves not only as capping ligand, but also as sulfur source for shell growth. Moreover, the CH_2 scissoring mode (1464 cm^{-1}) and the CH_3 symmetric bending vibration (1377 cm^{-1}) of DDT and the in-plane OH bending vibrations of OA[30] are observed. EDX analysis of the elemental composition of the $Zn_xCd_{1-x}S$:Mn/ZnS and $Zn_xCd_{1-x}S$:Mn dots shown in the *Supporting Information* (*SI*; Figures S1A and S1B) reveals Zn, S, Cd, and Mn peaks, with the growth of the ZnS shell around the $Zn_xCd_{1-x}S$:Mn core being reflected by an increased intensity of the Zn peak. The ratio between Zn and S increased from one in the $Zn_xCd_{1-x}S$:Mn cores to four in the core/shell $Zn_xCd_{1-x}S$:Mn/ZnS NCs.

Influence of NC growth parameters on PL properties. To optimize the PL properties of our NCs, we assessed different reaction parameters including temperature, ratio of the metal ion precusors, dopant ion concentration, and shell thickness. Crystal formation and NC growth due to the decomposition of the metalloorganic complexes starts at about 125 °C as indicated by a change in color of the solution from colorless to yellow and then to light orange.[31] This was confirmed by absorption and emission measurements summarized in Figure 3. The broad shoulder in the absorption spectrum at ca. 400 nm (Figure 3b, left axis), which undergoes a small red shift from 400 to 404 nm with increasing reaction time, is assigned to the first excitonic transition of the $Zn_xCd_{1-x}S$ NCs. Such a poorly resolved excitonic absorption peak is characteristic for ternary and quaternary alloyed NCs. Its width points to a wide size distribution and the irregular composition distribution.[4] The more or less constant spectral shape during a growth period of 3 h indicates no significant changes in alloy composition. The NCs extracted at 150 °C showed already a bright emission (Figure 3a). The highest emission intensity was revealed by samples taken at 230 °C (time “0” at the y-axis in Figure 3a). Longer reaction times and hence, further NC growth resulted in a rapid decrease in emission intensity. Figure 3b (Figure 3b, right axis) summarizes the corresponding emission spectra, which are not normalized to better visualize changes in spectral shape and PL intensity with temperature and reaction time. These spectra contain the characteristic $^4T_1$–$^6A_1$ emission of Mn^{2+} (see inset in Figure 3h) with its maximum at 598 nm, matching the values reported for ZnCdS:Mn materials with zinc-blende[23] as well as wurtzite crystal structure,[11] and a broad red PL band located at about 710 nm. The latter is attributed to emission from defect states or Mn^{2+} ions at or near the surface in ZnCdS:Mn.[32,33] Due to the "self-purification" effect,[12] a relatively large number of Mn^{2+} ions can be located in the vicinity of the surface in these NCs after long annealing times at 230 °C, which may account also for the reduction of the Mn^{2+} PL intensity in Figure 3a. The intensity of the long wavelength band at 150 °C is rather high for doped NCs as a homogeneous Mn^{2+} distribution can be expected under these reaction conditions. Thus, an additional contribution from the emission of Cd^{2+} species due to local inhomogeneity cannot be excluded. For example, an extrinsic deep-level emission at about 710 nm has been also reported for CdS,[23,33] which disappeared after coating of the NCs with a ZnS shell.

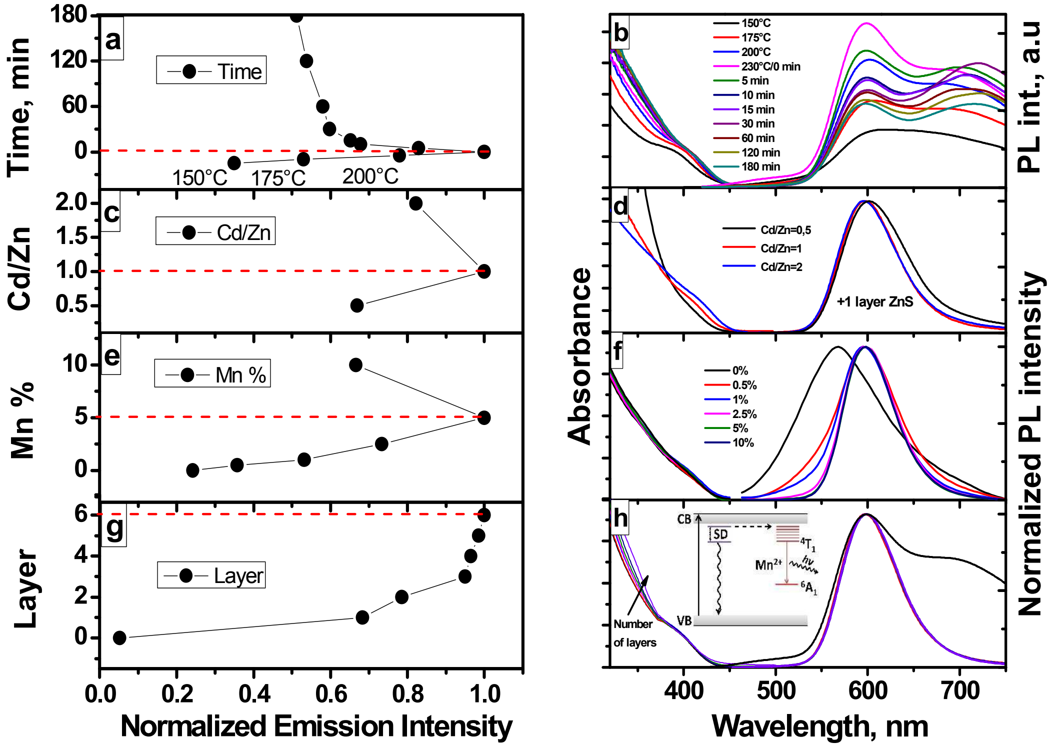

Figure 3. (a) Dependence of the intensity of the Mn^{2+} emission at 598 nm on reaction time and temperature. The PL intensities are normalized to the maximal Mn^{2+} PL intensity of the NCs taken from the reaction mixture directly after reaching 230 °C. (b) Thermal and temporal evolution of absorption (left axis)

and emission spectra (right axis) of (unshelled) $Zn_{0.5}Cd_{0.5}S$ NCs doped with 5 mol % of Mn^{2+} using excitation wavelengths (λ_{ex}) of 375 and 390 nm for the sample taken at 150°C and 175 °C, respectively, and 400 nm for all other samples to always excite each sample at the first excitonic absorption maximum. (c) PL intensity at different Cd/Zn precursor ratios and (d) the corresponding absorption (left axis) and normalized emission (right axis, excitation at the first excitonic absorption maximum of each sample) spectra of $Zn_{1-x}Cd_xS$:Mn/ZnS NCs. For all core compositions in panels c, d, e, and f, the NCs were coated with one layer of ZnS. (e) PL intensity of undoped $Zn_{0.5}Cd_{0.5}S$/ZnS and $Zn_{0.5}Cd_{0.5}S$/ZnS doped with different Mn^{2+} concentrations (λ_{ex} = 400 nm); (f) absorption (left axis) and normalized emission spectra (right axis) of undoped $Zn_{0.5}Cd_{0.5}S$/ZnS and Mn^{2+}-doped NCs. (g) Dependence of the PL intensity on the number of ZnS coating layers, and (h) evolution of the corresponding absorption (left axis) and normalized emission spectra (right axis, λ_{ex} = 400 nm) of the $Zn_{0.5}Cd_{0.5}S$:Mn core (black curve) and $Zn_{0.5}Cd_{0.5}S$:Mn/ZnS core-shell particles, doped with 5 mol % Mn^{2+}. All absorption spectra were recorded with samples having the same absorbance at the first excitonic absorption band/transition. The inset in panel (h) illustrates the light absorption associated with the valence band-conduction band transition, energy transfer from the accordingly formed exciton to the Mn^{2+} ions, and the nonradiative relaxation initiated by surface defects (SD). All measurements were performed with NCs dispersed in chloroform.

Cd/Zn molar ratio. To study the effect of the Cd/Zn molar ratio on the incorporation of Mn^{2+} into the crystal lattice and the optical properties of the resulting $Zn_xCd_{1-x}S:Mn^{2+}$/ZnS NCs, we prepared samples with Cd/Zn ratios of 0.5, 1, and 2, respectively and kept the concentration of the Mn^{2+} precursor in the reaction mixture constant at 5 mol %. Subsequently, the NCs were coated with a single layer of ZnS by addition of the Zn precursor to the reaction mixture at 230°C, see *Experimental* section.

As follows e.g., from Figure 3d, the absorption spectra measured at Cd/Zn ratios of 0.5, 1, and 2, respectively, reflect the change of the NC composition from Zn-rich to the Cd-rich samples by a red shift of the first excitonic maximum from ca. 395 to ca. 420 nm. The most intriguing change in emission is the suppression of the red PL at ca. 710 nm by the ZnS shell (Figure 3d, right axis). This underlines its origin from Mn^{2+} ions at or near the surface. Although the spectral position of the emission maximum of the Mn^{2+} (d^5) ion depends on crystal field,[34] the spectral shape and position of the emission band at 598 nm (Figure

3d, right axis), which arises from the $^4T_1$–$^6A_1$ transition of Mn^{2+} ions, is only slightly affected by the Cd/Zn ratio, with Zn-rich NCs (Cd/Zn ratio of 0.5) revealing a small red shift compared to Cd-rich NCs. This is in agreement with the data published by Chen et al.[27], Xua at al.,[35] and Kim et al.[24] The intensity of the Mn^{2+} emission is maximum for a Cd/Zn ratio of one (Figure 3c). This is consistent with the results reported by Nag et al.[11], who studied the influence of the Mn^{2+} concentration as a function of the lattice mismatch between MnS and $Zn_xCd_{1-x}S$ NCs and found an efficient incorporation of Mn^{2+} ions into the wurtzite host lattice of $Zn_xCd_{1-x}S$ for a Cd/Zn ratio of one. This seems to be also true for $Zn_xCd_{1-x}S$ NCs with a zinc blende structure as predicted by Klimov et al.,[36] because the enthalpy of Mn^{2+} ion doping is minimized at this NC composition.

Dopant ion concentration. The dependence of the PL intensity of the Mn-doped $Zn_xCd_{1-x}S$/ZnS (x = 0.5) NCs on Mn^{2+} concentration of is summarized in Figure 3e for concentrations of the Mn-precursor of 0.5 % to 10 % and the corresponding absorption and normalized emission spectra are shown in Figure 3f. The presence and the oxidation state of Mn^{2+} was confirmed by **EDX** and **XPS** measurements (*SI*, Figures S4, S1A, S1B). Doping of $Zn_xCd_{1-x}S$/ZnS (x = 0.5) NCs with increasing concentrations of Mn^{2+} barely affects the absorption spectra of these materials, which are dominated by optical transitions of the host matrix (first excitonic transition and band-band transitions) in contrast to the emission spectra and especially the PL intensity. As shown in Figure 3f, incorporation of Mn^{2+} shifts the initially broad emission of the undoped $Zn_xCd_{1-x}S$ QDs, originating from a broad distribution of shallow trapped states,[37,33] to 598 nm, i.e., to the typical Mn^{2+} emission band, and leads to a narrowing of the PL band with increasing Mn^{2+} concentration. The highest PL intensity is reached for samples grown from stock solutions containing 5 mol. % of the Mn precursor (Figure 3e). Higher dopant ion concentrations lead to a decrease in PL intensity. This reflects two processes, the incorporation of the Mn^{2+} ions into the crystal lattice of the NCs, acting as luminescence centers, and a concentration quenching at higher Mn^{2+} doping concentrations due to energy transfer and energy migration between neighboring Mn^{2+} ions, with Mn^{2+} ions located at or near the surface acting as energy sinks. Concentration quenching in d-dots has been reported also by other groups.[11, 38] For example, Nag et al.[11] observed maximum PL intensities for unshelled $Zn_{0.49}Cd_{0.51}S$:Mn doped with about 1 % Mn^{2+} and Kole et al.[38] realized maximum PL intensities of unshelled ZnS d-dots with a Mn^{2+}

doping concentration of 1.1 %. We ascribe our observation of Mn^{2+} concentration quenching at considerably higher dopant ion concentrations to the protecting ZnS shell of our NCs, which shields surface or near surface Mn^{2+} ions. Also, Mn^{2+} ions may partially diffuse into the shell during its formation, which affects Mn^{2+}-Mn^{2+} distances and hence, energy transfer and energy migration between neighboring Mn^{2+} ions.

Influence of ZnS shell thickness. A common approach to increase Φ_{pl} of binary or ternary semiconductor NCs such as CdSe,[39] CdTe,[40] $CuInS_2$[41,42,43] and d-dots like ZnCdS:Mn,[27] $Zn_{1-x-y}Cd_xMn_yS$[7] and ZnSe:Mn[44] presents the shelling of their surface with a higher band gap semiconductor (e.g., ZnS, CdS) or with more sophisticated multi-shells like ZnS/CdS[23] or CdS/$Zn_{0.5}Cd_{0.5}S$/ZnS[5] to passivate dangling bonds and surface states favoring radiationless decay or emission with low intensity from trapped states. The beneficial influence of a surface shell follows also from Figures 3c and 3d depicting the influence of a single shell on the PL properties of our $Zn_xCd_{1-x}S$:Mn NCs. For maximum $\Phi_{pl,,}$[45,46] the shell thickness needs to be optimized material-specifically. Hence, we studied the influence of the ZnS shell thickness on the PL intensity of already optimized d-dots, here $Zn_{0.5}Cd_{0.5}S$:Mn cores (Zn/Cd ratio of 1:1), doped with 5 mol % Mn. For this purpose, shelling with ZnS was performed in a simple one pot reaction at 230 °C by stepwise injection of identical amounts of a stock solution of the Zn precursor in time intervals of 15 min. At this temperature the alloying effect is absent. Zhong and co-workers[59] defined 270 °C as the "alloying point" analogous to melting or boiling points, for the CdSe/ ZnSe and CdSe/ZnS systems. Below this temperature the alloying process between core and shell is energetically disadvantageous. The ZnS shell grown in these 15 min is considered as one layer. The corresponding absorption and normalized emission spectra and the resulting PL intensities are summarized in Figures 3g and 3h, respectively. The growth and increasing thickness of the ZnS shell is confirmed by the increasing absorption in the UV region of 320 to 370 nm (Figure 3h) and the disappearance of the red emission at 710 nm (Figures 3b and 3h). Additional proof for the ZnS shell is the increased Zn content in the core/shell NCs when compared to the uncoated core. Both, EDX and XPS spectra confirm an enhancement of the Zn/Cd ratio for the core/shell particles (*SI*, Figures S4, S1A, S1B), and the prolongation of the photoluminescence lifetime from 0.89 to 2.85 ms, does not allow any other conclusion than the formation of a ZnS shell acting as effective surface passivation layer (Figure 4). The spectral position of the Mn^{2+} emission is independent of the number of ZnS layers, whereas its intensity strongly increases with shell thickness. A single ZnS layer enhances the PL intensity of the $Zn_{0,5}Cd_{0,5}S$ core, showing a Φ_{pl} below 4%, already by a factor of 14 (Figure 3g). The photoluminescence decay curves of $Zn_{0.5}Cd_{0.5}S$:Mn and $Zn_{0.5}Cd_{0.5}S$:Mn/ZnS nanocrystals are shown in Figure 4. The intensity average lifetime τ, given by:

$$\tau = \frac{\int tI(t)dt}{\int I(t)dt}, \qquad (2)$$

is 0.89 ms for $Zn_{0.5}Cd_{0.5}S$:Mn particles and 2.85 ms for the $Zn_{0.5}Cd_{0.5}S$:Mn/ZnS particles, giving evidence of the effective passivation of surface defects for the ZnS-coated sample. To the best of our knowledge, such a long excited-state carrier lifetime is highest reported for the ZnS and Cd based Mn^{2+} doped NCs (see SI, Table S1).

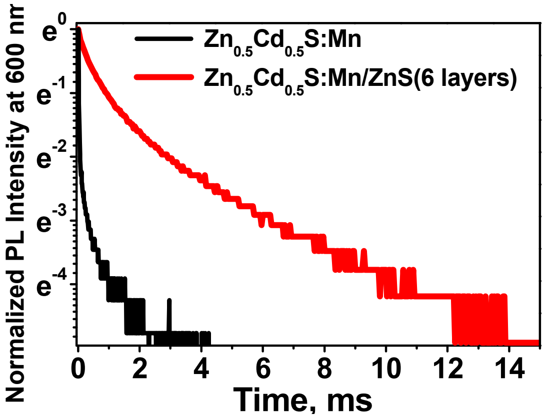

Figure 4. PL decay curves of the $Zn_{0.5}Cd_{0.5}S$:Mn and $Zn_{0.5}Cd_{0.5}S$:Mn/ZnS NCs with six Zn precursor injection. Chloroform solutions of the NCs exited with Xe-lamp at 320 nm, and detection wavelength at 600 nm for both samples.

The highest Φ_{pl} achieved for our core-shell NCs with this strategy amounts to 70 %. This Φ_{pl} is the highest values reported for Mn^{2+}-doped sulfide-semiconductor NCs, [6,9,17, 21, 24,27,35,36] (*also* see *SI*, Table S1) that were, however, prepared using much more sophisticated synthetic schemes as our simple one pot reaction.

Up-scaling. Use of doped NCs e.g., for the fabrication of more efficient solar cells or other opto-electronic devices requires synthetic procedures that efficiently and reproducibly yield a large amount of high quality NC material. We subsequently studied the upscaling of our simple one pot, two step synthesis of $Zn_{0.5}Cd_{0.5}S$:Mn/ZnS with optimum luminescence properties. Hence, the amount of all components was increased by a factor of 40 compared to the initially used synthesis (see *Experimental* section). This allowed for the preparation of 3.5 g of $Zn_{0.5}Cd_{0.5}S$:Mn/ZnS NCs in identical quality (Figure S3, *SI*).

Mn^{2+}-doped $Zn_xCd_{1-x}S$/ZnS NCs as converter material in Si solar cells. To demonstrate the application potential of our optimized Mn^{2+}-doped $Zn_xCd_{1-x}S$/ZnS NCs, we employed this material as UV-to-visible light converter in monocrystalline silicon (mono-Si) solar cells to improve the otherwise low sensitivity of mono-Si solar cells in the UV and blue spectral region by shifting the energy of these otherwise unused photons to a spectral region of higher sensitivity of the mono-Si cell[47]. Semiconductor NCs like CdSe/CdS, ZnSe, CdSe/ZnSe, $Zn_{0.5}Cd_{0.5}S$/ZnS have been already used as effective UV-light converter materials for downshifting layers[48,49,50,51], yet not ternary Mn-doped NCs. The scheme of the down-shifting mechanism and a schematic representation of our proof-of-concept converter film - mono-Si-solar cell system are shown in Figure 5a.

For this purpose, we dispersed $Zn_{0.5}Cd_{0.5}S$:Mn(5%)/ZnS NCs with Φ_{pl} of 70% in toluene in different concentrations of 0.5, 1, 2.5, 5, 10, 15, 20, 25 mg/ml and coated a thin film on a commercial mono-Si solar cell with a SiN_x coated texture by the doctor blade technique. Subsequently, the resulting three solar cells were dried on a hot plate at 80 °C for five minutes. Then, the external quantum efficiency (EQE), i.e. the number of charge carriers to the number of incident photons ratio, and the current density (J)–voltage (V) curves (J-V diagrams) of the three solar cells depicted in Figure 5a (right panel) were measured. The open-circuit voltage (U_{OC}) and fill factor (FF; FF = max. power/J_{SC} U_{OC}) are taken from the J-V measurements under the solar simulator, the short circuit current (J_{SC}) was calculated from the EQE spectra, and after that the power conversion efficiency (PCE) was calculated. This is necessary, because due to the deviation of the spectrum of the solar simulator from the standard AM1.5G spectrum (much weaker emission at wavelengths below 400 nm), it is not possible to use the solar simulator for the characterization of the downshifting layers covered solar cells.

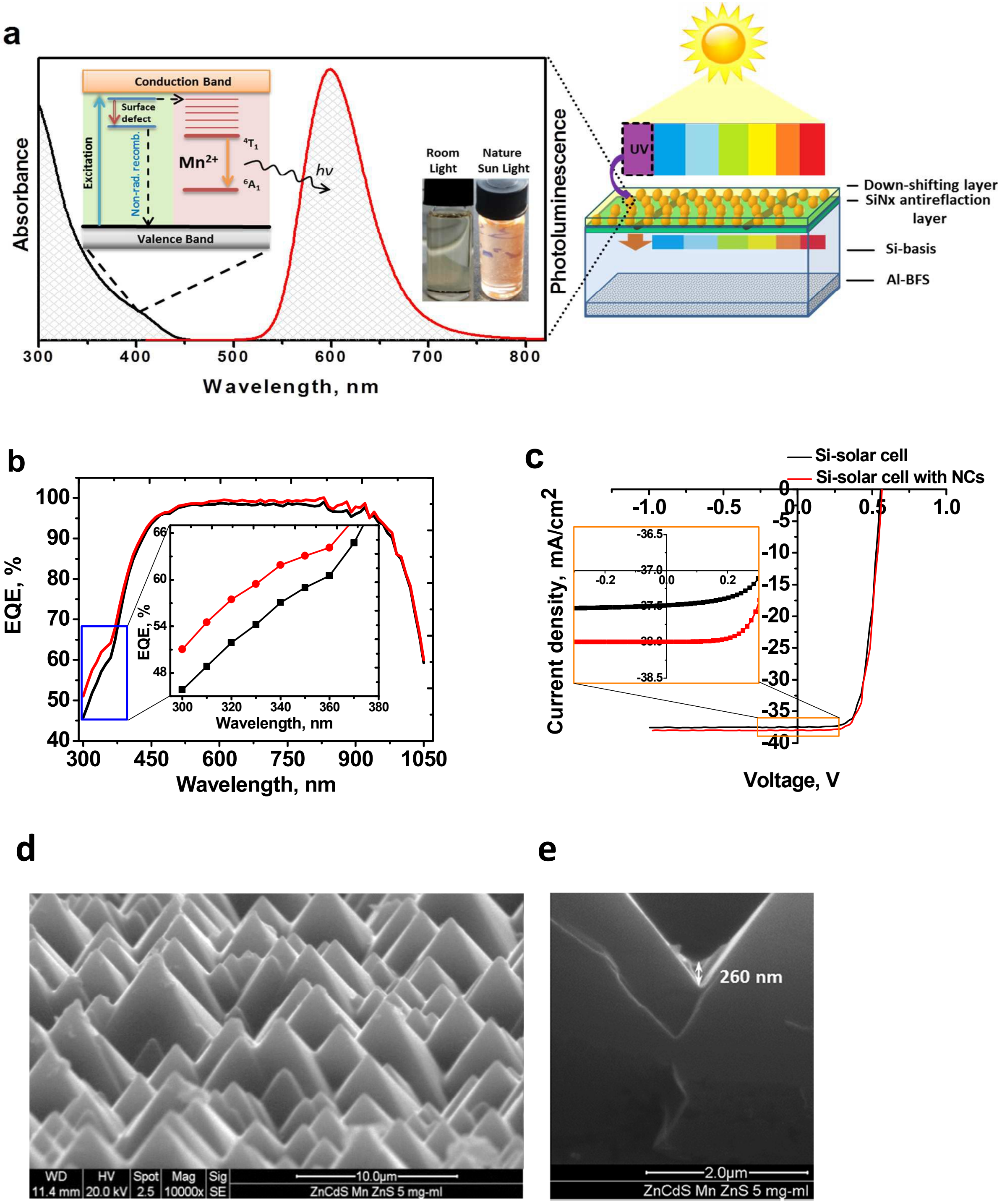

Figure 5. Performance of mono-Si solar cells coated with $Zn_{0.5}Cd_{0.5}S$:Mn(5%)/ZnS NCs, using a volume 200 μl of the differently concentrated NCs dispersion. (a) Scheme of the down-shifting mechanism of the $Zn_{0.5}Cd_{0.5}S$:Mn(5%)/ZnS NC converter material and design of proof-of-concept solar cells. (b) EQE of the

best mono-Si solar cell (black curve) obtained with a $Zn_{0.5}Cd_{0.5}S$:Mn(5%)/ZnS NC dispersion containing 10 mg/ml NCs (red curve); the EQE in the wavelength region of 300 to 400 nm is magnified in the inset. (c) J–V curves of the corresponding solar cells. . (d) SEM picture of the mono-Si solar cell surface structure coated with 5 mg/ml NCs solution. (e) cross-section of the same mono-Si solar cell with 260 nm NCs thickness.

Measurement of the EQE curves of the mono-Si solar cells coated with different concentrations of $Zn_{0.5}Cd_{0.5}S$:Mn(5%)/ZnS NCs (Figures 5b, S5A-S11A in the *SI*) reveal an increased EQE in the range of 0.5-15 mg/ml (Figures 5b and S5A-S9A in the *SI*) and a significantly decreased EQE for higher concentrations of 20-25 mg/ml due to parasitic absorption by the thicker NC layer (*SI*, Figures S10A and S11A). The optimized performance with an EQE enhancement of 12 % is found for the layers coated form a 10 mg/ml concentrated solution (Figure 5b).

The average thickness of the NCs layer was determined by SEM cross section measurements and yielded values between <50 nm to 750 nm (Figure 5e and S12 A-E in the *SI*) for the various concentrations. The best performing coating from the 10 mg/ml concentrated solution showed a layer thickness of 300 nm (Figure S12C) at an EQE enhancement of app. 12 % as shown in Figure 6.

We also observed an enhancement of the EQE in the visible and in the NIR region, here mostly due to the NCs acting as antireflection coating on SiN_x, as the refractive indexes of ZnCdS and SiN_x equal 1.95[52] and 2.0, respectively.

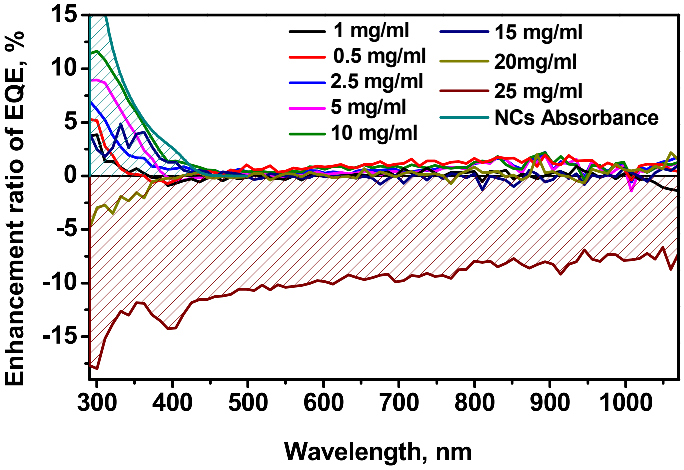

Figure 6. Enhancement ratio of EQE of mono-Si solar cells as function of wavelength for the coating with differently concentrated $Zn_{0.5}Cd_{0.5}S$:Mn(5%)/ZnS NCs dispersions.

The results of the measurements of the current density (J) –voltage (V) curves (J-V diagrams) are shown in Figure 5c and in Figures S5B-S11B in the *SI*. Lower concentrated solution with 0.5-15 mg/ml (Figures 5c and S5A-S8A in the *SI*) led to an increase in power conversion efficiency (PCE) and in short circuit current (J_{SC}), demonstrating the down-shifting effect of our NCs. For the best sample of the mono-Si solar cell coated with 10 mg/ml, PCE led to an enhancement by nearly 0.5 percentage points, which is close to theoretical limit (0.6%) of the down-shifting layer for Si solar cell [47].

The electrical characteristics of the solar cells coated with $Zn_{0.5}Cd_{0.5}S$:Mn(5%)/ZnS NCs are summarized in Table 2.

Table 2. Photovoltaic properties of mono-Si solar cells coated with differently concentrated dispersions of $Zn_{0.5}Cd_{0.5}S$:Mn(5%)/ZnS NCs. Open-circuit voltage (U_{OC}) and fill factor (FF; FF = max. power/J_{SC} U_{OC}) are taken from the J-V measurements under the solar simulator, the short circuit current (J_{SC}) and the power conversion efficiency (PCE) are calculated from the EQE spectra.

Sample		U_{oc} (V)	FF, %	J_{sc} (mA/cm^2)	PCE, %	Δ PCE, %
1	Solar cell Solar cell + 0.5mg/ml QDs	0,522±0,0114 0,528±0,0116	64,69±0,2504 64,70±0,8163	35,979±0,0184 35,950±0,0184	12.149±0,0448 12.281±0,0175	+ 0,132
2	Solar cell Solar cell + 1 mg/ml QDs	0,536±0,0117 0,537±0,0118	63,63±0,8346 64,52±0,6900	35,209±0,0180 35,531±0,0182	12.008±0,1669 12.310±0,1083	+ 0,302
3	Solar cell Solar cell + 2.5mg/ml QDs	0,538±0,0118 0,545±0,0119	64.59±0,9580 65.37±0,5120	38,061±0,0195 38,341±0,0196	13.225±0,1910 13.659±0,2490	+ 0,434
4	Solar cell Solar cell + 5 mg/ml QDs	0,538±0,0118 0,552±0,0121	65.14±1,151 65.14±0,605	38,414±0,0197 38,716±0,0198	13.463±0,224 13.921±0,149	+ 0,458
5	Solar cell Solar cell + 10 mg/ml QDs	0,546±0,0120 0,558±0,0122	65.60±0,622 65.81±0,754	38,499±0,0197 38,861±0,0199	13.809±0,109 14.271±0,268	+ 0,462
6	Solar cell Solar cell + 15 mg/ml QDs	0,546±0,0120 0,549±0,0120	65,47±0,7355 65,61±0,7580	36,033±0,0184 36,013±0,0184	12.880±0,3141 12.900±0,1433	+ 0.02
7	Solar cell Solar cell + 20 mg/ml QDs	0,534±0,0117 0,534±0,0117	65,86±0,1542 66,01±0,5872	35,866±0,0183 35,795±0,0183	12.613±0,2162 12.588±0,1913	- 0,025
8	Solar cell	0,538±0,0118	65,66±0,1443	35,857±0,0183	12.667±0,059	- 1,025

	Solar cell + 25 mg/ml QDs	0,540±0,0118	65,65±0,1443	32,570±0,0167	11.546±0,0427	

Although due to many research activities dedicated to new solar cells with improved efficiencies like perovskite, solar cells with an efficiency of more than 20%,[56] the broad use of photovoltaics requires strategies for the simple and inexpensive upgrading of the currently used Si photovoltaic modules to increase their power conversion efficiency without costly replacement. In this respect, and to underline the application potential of these novel down-shifting layers, we performed a simple BoM and BoS cost calculation for the fabrication of photovoltaic (PV) modules based on our down-shifting design and summarized the findings in the *SI*.. Based upon this estimation, we conclude that application of a thin layer of highly luminescent $Zn_{0.5}Cd_{0.5}S$:Mn/ZnS NCs (use of 0.2 ml of a dispersion of 2.5 mg/ml NC distributed on an area of 8 cm^2), can decrease the production costs of a one Watt energy for mono-Si solar module with power 117W by about 1.5 \$ (3.3 %) due to the enhanced efficiency in parallel to the unprecedented low costs of this novel converter material.

Conclusion and Outlook

In summary, we developed a simple one-pot two-step synthesis for high quality $Zn_xCd_{1-x}S$:Mn/ZnS NCs with a very high reproducibility. Very high photoluminescence quantum yields (Φ_{pl}) of up to 70 % and the ease of upscaling this industrially compatible fabrication process make this doped semiconductor material a very promising candidate especially for photovoltaic and optoelectronic applications including light-emitting devices. The potential of these NCs follows from the exemplarily shown use of the $Zn_{0.5}Cd_{0.5}S$:Mn(5%)/ZnS NCs as down-shifting layer for the ultraviolet (UV) to orange wavelength region for monocrystalline silicon (mono-Si) solar cells. With our NCs and a simple coating technique, the efficiency of a commercial Si solar cell could be improved up to ca. 12 % in the UV spectral region which led to an enhancement of PCE by nearly 0.5 percentage points. This allows a reduction of the production costs of mono-Si solar cell modules by around 3.33 %. Future work on these doped ternary alloys will focus on the further improvement of their Φ_{pl} and their use as down-shifting layer for different types of solar cells such as thin film, e.g. $CuInS_2$ or organic solar cells with a low sensitivity in the blue and UV spectral region, thereby paving the road for the next generation of more efficient and less costly photovoltaic modules for the broad use of solar energy.

Supporting Information Available: Energy-Dispersive X-ray Spectroscopy (EDX) data, measurements of EQE data and J-V curves, cost effective calculation etc.

Acknowledgement. This research was performed as part of the Energie Campus Nürnberg (EnCN) and supported by funding through the “Bavaria on the Move” initiative of the state of Bavaria and the project 1006-11 of the Bavaria Research Foundation (BFS). We gratefully acknowledge financial support from the Cluster of Excellence “Engineering of Advanced Materials” at the University Erlangen-Nürnberg and from the Federal Ministry for Economic Affairs and Energy (MNPQ program BMWI 11/12). We express our gratitude to Norman Lüchinger from Nanograde Ltd. for help in cost effective calculations and Alfons

Stiegelschmitt for XRD measurements. P.H. acknowledges financial support by the DFG through the research training group 1896 ‘‘In situ microscopy with electrons, X-rays and scanning probes’’. Electron microscopy resources have been kindly provided by the Center for Nanoanalysis and Electron Microscopy (CENEM). We express our gratitude to Alfons Stiegelschmitt for XRD measurements.

References

1. P. Wu and X.-P. Yan, Chemical Society Reviews, 2013, 42, 5489-5521.
2. N. Pradhan, D. Goorskey, J. Thessing and X. Peng, Journal of the American Chemical Society, 2005, 127, 17586-17587.
3. N. Pradhan and X. Peng, Journal of the American Chemical Society, 2007, 129, 3339-3347.
4. W. Zhang, X. Zhou and X. Zhong, Inorganic Chemistry, 2012, 51, 3579-3587.
5. R. Xie, U. Kolb, J. Li, T. Basché and A. Mews, Journal of the American Chemical Society, 2005, 127, 7480-7488.
6. R. W. Knoss, Nova Science, New York, 2009, 691.
7. L. R. Bradshaw, K. E. Knowles, S. McDowall and D. R. Gamelin, Nano Letters, 2015, 15, 1315-1323.
8. Y. Yang, O. Chen, A. Angerhofer and Y. C. Cao, Journal of the American Chemical Society, 2006, 128, 12428-12429.
9. U. Resch-Genger, M. Grabolle, S. Cavaliere-Jaricot, R. Nitschke and T. Nann, Nat Meth, 2008, 5, 763-775.
10. M. Grabolle, M. Spieles, V. Lesnyak, N. Gaponik, A. Eychmüller and U. Resch-Genger, Analytical Chemistry, 2009, 81, 6285-6294.
11. A. Nag, S. Chakraborty and D. D. Sarma, Journal of the American Chemical Society, 2008, 130, 10605-10611.
12. G. M. Dalpian and J. R. Chelikowsky, Physical Review Letters, 2006, 96, 226802.
13. P. I. Archer, S. A. Santangelo and D. R. Gamelin, Journal of the American Chemical Society, 2007, 129, 9808-9818.
14. F. V. Mikulec, M. Kuno, M. Bennati, D. A. Hall, R. G. Griffin and M. G. Bawendi, Journal of the American Chemical Society, 2000, 122, 2532-2540.
15. J. F. Suyver, S. F. Wuister, J. J. Kelly and A. Meijerink, Physical Chemistry Chemical Physics, 2000, 2, 5445-5448.
16. D. J. Norris, N. Yao, F. T. Charnock and T. A. Kennedy, Nano Letters, 2001, 1, 3-7.
17. P. V. Radovanovic and D. R. Gamelin, Journal of the American Chemical Society, 2001, 123, 12207-12214.
18. R. Zeng, T. Zhang, G. Dai and B. Zou, The Journal of Physical Chemistry C, 2011, 115, 3005-3010.
19. R. Zeng, M. Rutherford, R. Xie, B. Zou and X. Peng, Chemistry of Materials, 2010, 22, 2107-2113.

20. K.-H. Lee, J.-H. Lee, W.-S. Song, H. Ko, C. Lee, J.-H. Lee and H. Yang, ACS Nano, 2013, 7, 7295-7302.
21. P. Samokhvalov, M. Artemyev and I. Nabiev, Chemistry – A European Journal, 2013, 19, 1534-1546.
22. S. Cao, C. Li, L. Wang, M. Shang, G. Wei, J. Zheng and W. Yang, Sci. Rep., 2014, 4.
23. S. Cao, J. Zheng, J. Zhao, L. Wang, F. Gao, G. Wei, R. Zeng, L. Tian and W. Yang, Journal of Materials Chemistry C, 2013, 1, 2540-2547.
24. K. Jong-Uk, L. Myung-Hyun and Y. Heesun, Nanotechnology, 2008, 19, 465605.
25. C. S. Erickson, L. R. Bradshaw, S. McDowall, J. D. Gilbertson, D. R. Gamelin and D. L. Patrick, ACS Nano, 2014, 8, 3461-3467.
26. F. Meinardi, A. Colombo, K. A. Velizhanin, R. Simonutti, M. Lorenzon, L. Beverina, R. Viswanatha, V. I. Klimov and S. Brovelli, Nat Photon, 2014, 8, 392-399.
27. Z.-Q. Chen, C. Lian, D. Zhou, Y. Xiang, M. Wang, M. Ke, L.-B. Liang and X.-F. Yu, Chemical Physics Letters, 2010, 488, 73-76.
28. M. Luo, G. K. Olivier and J. Frechette, Soft Matter, 2012, 8, 11923-11932.
29. D. Xu, Z. Liu, J. Liang and Y. Qian, The Journal of Physical Chemistry B, 2005, 109, 14344-14349.
30. J. Yang, T. Ling, W.-T. Wu, H. Liu, M.-R. Gao, C. Ling, L. Li and X.-W. Du, Nat Commun, 2013, 4, 1695.
31. Y. Vahidshad, M. Nawaz Tahir, A. Iraji Zad, S. M. Mirkazemi, R. Ghasemzadeh, H. Huesmann and W. Tremel, The Journal of Physical Chemistry C, 2014, 118, 24670-24679.
32. Hazarika, A. Layek, S. De, A. Nag, S. Debnath, P. Mahadevan, A. Chowdhury and D. D. Sarma, Physical Review Letters, 2013, 110, 267401.
33. Y. Chen, X. Zhang, C. Jia, Y. Su and Q. Li, The Journal of Physical Chemistry C, 2009, 113, 2263-2266.
34. G. Blasse and B. C. Grabmaier, in *Luminescent Materials*, Springer Berlin Heidelberg, 1994, DOI: 10.1007/978-3-642-79017-1_3, ch. 3, pp. 33-70.
35. W. Xu, X. Meng, W. Ji, P. Jing, J. Zheng, X. Liu, J. Zhao and H. Li, Chemical Physics Letters, 2012, 532, 72-76.
36. B. Rémi, T. O. Stefan and R. G. Daniel, in *Nanocrystal Quantum Dots, Second Edition*, CRC Press,2010, DOI: 10.1201/9781420079272-c11, pp. 397-453.
37. J. Ouyang, C. I. Ratcliffe, D. Kingston, B. Wilkinson, J. Kuijper, X. Wu, J. A. Ripmeester and K. Yu, The Journal of Physical Chemistry C, 2008, 112, 4908-4919.
38. K. Kole, C. S. Tiwary and P. Kumbhakar, Journal of Applied Physics, 2013, 113, 114308.

39. D. V. Talapin, R. Koeppe, S. Götzinger, A. Kornowski, J. M. Lupton, A. L. Rogach, O. Benson, J. Feldmann and H. Weller, Nano Letters, 2003, 3, 1677-1681.
40. W. Zhang, G. Chen, J. Wang, B.-C. Ye and X. Zhong, Inorganic Chemistry, 2009, 48, 9723-9731.
41. W. Zhang and X. Zhong, Inorganic Chemistry, 2011, 50, 4065-4072.
42. R. Xie, M. Rutherford and X. Peng, Journal of the American Chemical Society, 2009, 131, 5691-5697.
43. L. Li, T. J. Daou, I. Texier, T. T. Kim Chi, N. Q. Liem and P. Reiss, Chemistry of Materials, 2009, 21,
44. F. Zheng, W. Ping, Z. Xinhua and Y. Yong-Ji, Nanotechnology, 2010, 21, 305604.
45. Coropceanu and M. G. Bawendi, Nano Letters, 2014, 14, 4097-4101.
46. B. O. Dabbousi, J. Rodriguez-Viejo, F. V. Mikulec, J. R. Heine, H. Mattoussi, R. Ober, K. F. Jensen and M. G. Bawendi, The Journal of Physical Chemistry B, 1997, 101, 9463-9475.
47. C. P. Thomas, A. B. Wedding and S. O. Martin, Solar Energy Materials and Solar Cells, 2012, 98, 455-464.
48. S. Kalytchuk, S. Gupta, O. Zhovtiuk, A. Vaneski, S. V. Kershaw, H. Fu, Z. Fan, E. C. H. Kwok, C.-F. Wang, W. Y. Teoh and A. L. Rogach, The Journal of Physical Chemistry C, 2014, 118, 16393-16400.
49. J.-Y. Jung, K. Zhou, J. H. Bang and J.-H. Lee, The Journal of Physical Chemistry C, 2012, 116, 12409-12414.
50. S.-W. Baek, J.-H. Shim, H.-M. Seung, G.-S. Lee, J.-P. Hong, K.-S. Lee and J.-G. Park, Nanoscale, 2014, 6, 12524-12531.
51. S.-W. Baek, J.-H. Shim and J.-G. Park, Physical Chemistry Chemical Physics, 2014, 16, 18205-18210.
52. S. Singhal, A. K. Chawla, H. O. Gupta and R. Chandra, Thin Solid Films, 2009, 518, 1402-1406.
53. C. K. Huang, Y. C. Chen, W. B. Hung, T. M. Chen, K. W. Sun and W. L. Chang, Progress in Photovoltaics: Research and Applications, 2013, 21, 1507-1513.
54. C. Würth, J. Pauli, C. Lochmann, M. Spieles and U. Resch-Genger, Analytical Chemistry, 2012, 84, 1345-1352.
55. C. Würth, M. Grabolle, J. Pauli, M. Spieles and U. Resch-Genger, Nat. Protocols, 2013, 8, 1535-1550.
56. W. S. Yang, J. H. Noh, N. J. Jeon, Y. C. Kim, S. Ryu, J. Seo and S. I. Seok, Science, 2015, 348, 1234-1237.
57. M. Tsuji, D. Yamaguchi, M. Matsunaga and M. J. Alam, Crystal Growth & Design, 2010, 10, 5129-5135.
58. X. Li, D. Shen, J. Yang, C. Yao, R. Che, F. Zhang and D. Zhao, *Chemistry of Materials*, 2013, 25, 106-112.

59. X. Zhong, M. Han, Z. Dong, T. J. White and W. Knoll, *Journal of the American Chemical Society*, 2003, 125, 8589-8594.

TOC Graphical Abstract

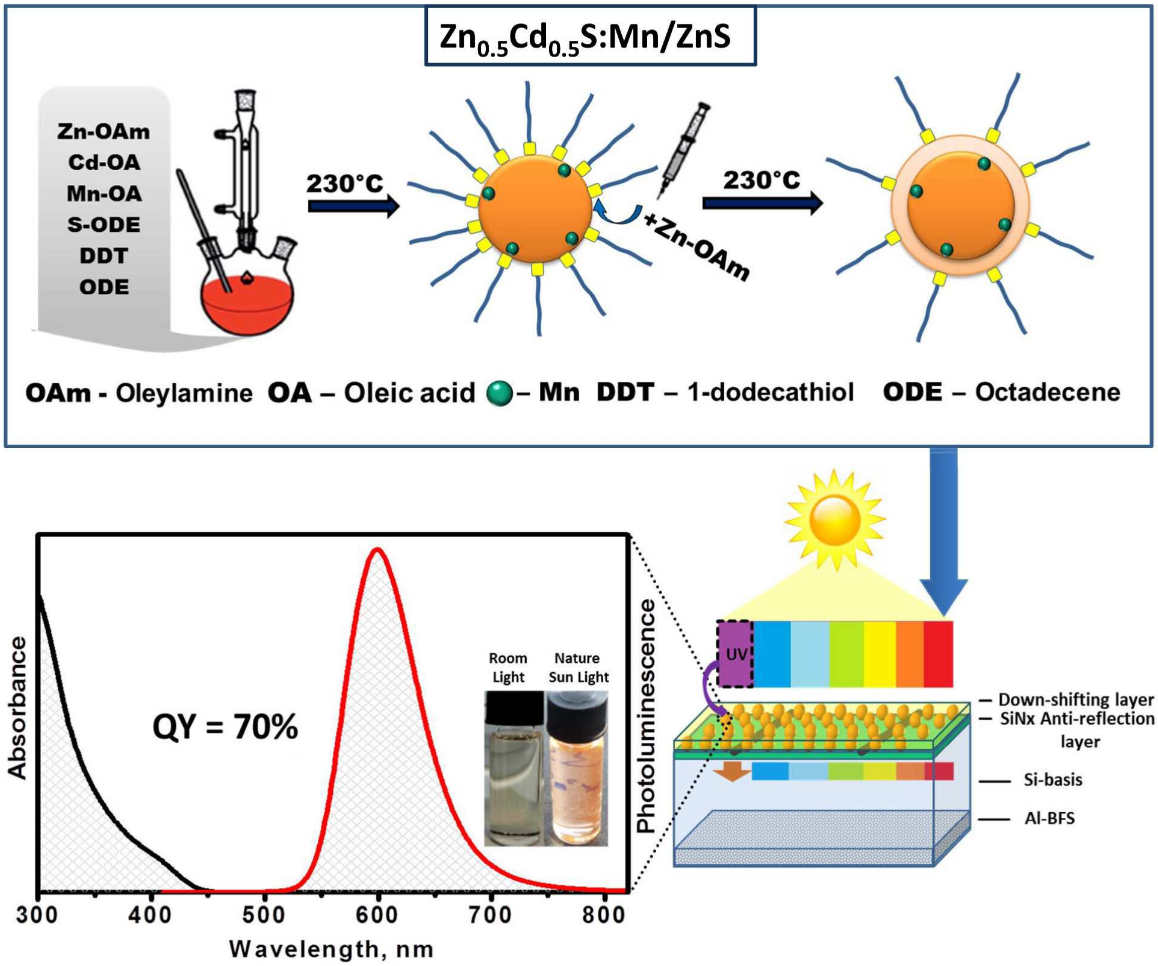

Broader context

The low efficiencies of inorganic solar cells in the ultraviolet (UV) and blue spectral region are key factors which restrict their power conversion efficiency (PCE). A simple and reliable technological step to overcome these limitations, which can be easily introduced into the manufacturing process, is the coating of the cover glass or the solar cells/modules by a light-converting material with high absorption in the UV-blue, luminescence in the active solar cell region, and a high photoluminescence quantum yield / efficiency. The resulting conversion of UV/blue light to the active spectral region of the solar cell, can improve PCE by several percentage points, especially in the case of thin-film solar cells based on $CuInGaSe_2$ or CdTe. Due to the already relatively high efficiency of the monocrystalline silicon (mono-Si) solar cells in the UV (about 45 % at 300 nm) the expected improvement of the PCE of these cells is about 0.6 percentage points. Due to the high market share of the mono-Si modules, this improvement is expected to be nevertheless very profitable. To demonstrate the potential of this concept using the most promising type of light converters, zero-reabsorption doped semiconductor quantum dots (QDs) , we developed a simple non-injection one-pot, two-step synthetic route to $Zn_xCd_{1-x}S$:Mn/ZnS core-shell nanocrystals showing a broad and efficient emission centered at 598 nm, that can be easily upscaled, and a simple coating technique to generate down shifting layers applicable to conventional mono-Si solar cells. With this approach, we could improve the efficiency of a commercial Si solar cell by up to ca. 12 % in the UV spectral region which led to an enhancement of PCE by nearly 0.5 percentage points and will enable a cost reduction of ca. 3.3%. Our simple strategy is expected to encourage solar module manufacturers to also equip their photovoltaic modules with light converting layers and pave the road to a broader application of solar cells.